ELSEVIER

Journal of Biomechanics 40 (2007) 427–436

JOURNAL OF BIOMECHANICS

www.elsevier.com/locate/jbiomech
www.JBiomech.com

The influence of vessel wall elasticity and peripheral resistance on the carotid artery flow wave form: A CFD model compared to in vivo ultrasound measurements

N.M. Maurits[a,*], G.E. Loots[b], A.E.P. Veldman[b]

[a]*Department of Neurology, University Medical Center Groningen, V4, P.O. Box 30.001, 9700 RB Groningen, The Netherlands*
[b]*University of Groningen, Institute of Mathematics and Computing Science, P.O. Box 800, 9700 AV Groningen, The Netherlands*

Accepted 14 December 2005

Abstract

The Doppler flow wave form and its derived measures such as the pulsatility index provide clinically important tools for the investigation of arterial disease. The typical shape of Doppler flow wave forms is physiologically known to be largely determined by both peripheral resistance and elastic properties of the arterial wall.

In the present study we systematically investigate the influence of both vessel wall elasticity and peripheral resistance on the flow wave form obtained from a CFD-simulation of blood flow in the carotid bifurcation. Numerical results are compared to in vivo ultrasound measurements. The in vivo measurement provides a realistic geometry, local elasticities and an input flow wave form for the numerical experiment.

Numerical and experimental results are compared at three different sites in the carotid branches. Peripheral resistance has a profoundly decreasing effect on velocities in the external carotid artery. If elasticity is taken into account, the computed peak systolic velocities are considerably lower and a more realistic smoothing of the flow wave form is found. Together, the results indicate that only if both vessel wall elasticity and positive peripheral resistance are taken into account, experimentally obtained Doppler flow wave forms can be reproduced numerically.

Keywords: Carotid bifurcation; Elasticity; Peripheral resistance; Flow wave form; Numerical simulation

1. Introduction

Atherosclerosis of the carotid arteries is a major cause of ischemic cerebrovascular accidents. Different studies have shown that atherosclerotic sites correlate strongly with regions of disturbed flow (see Ross, 1993; Ku, 1997; Kleinstreuer et al., 2001 for overviews). However, the precise hemodynamic determinants of atherosclerotic disease are not yet completely understood.

In the last decades computational fluid dynamics (CFD) studies have greatly enlarged our knowledge of hemodynamic factors involved in atherogenesis (Kleinstreuer et al., 2001; Ku, 1997). Only recently, have CFD results been directly compared to hemodynamic flow parameters obtained in vivo (Long et al., 2000; Milner et al., 1998; Moore et al., 1999; Zhao et al., 2000; Cebral et al., 2002). Validated CFD models can be very valuable in the early detection of vessels at risk and the prediction of future disease progression.

Of the currently available measurement techniques, duplex ultrasound imaging is a quick, non-invasive, safe and relatively cheap method to visualize arterial geometry and flow in vivo (von Reutern and von Büdingen, 1993). Clinically, some characteristics of the (Doppler) flow wave form, such as systolic, mean and diastolic velocities and the pulsatility index (PI = (systolic velocity−diastolic velocity)/(mean velocity)), are

*Corresponding author. Tel.: +31 50 3612411; fax: +31 50 3611707.
E-mail address: n.m.maurits@neuro.umcg.nl (N.M. Maurits).

0021-9290/$ - see front matter © 2006 Elsevier Ltd. All rights reserved.
doi:10.1016/j.jbiomech.2005.12.008

employed. These parameters are used to discern the different vessels, to assess vessel wall elasticity, the presence of distal stenoses, generalized downstream pressure increase, and generalized loss of elasticity. The PI was found to be linearly related to peripheral resistance, independent of flow and pressure. This further supports its clinical use (Legarth and Thorup, 1989; Legarth and Nolsoe, 1990).

Even in healthy subjects, the waveforms in the common (CCA), internal carotid artery (ICA) and external carotid artery (ECA) have different shapes, due to higher peripheral resistance in the arteries supplied by the ECA compared to the ICA and decreasing elasticity with distance from the bifurcation in the ICA- and ECA-branches compared to the CCA (Reneman et al., 1996).

To our knowledge, the combined influence of peripheral resistance and vessel wall elasticity on CFD results has not yet been studied. However, CFD flow parameters obtained from rigid and elastic carotid wall models, keeping all other parameters the same, have been compared. Typically, in the elastic models, a considerable reduction in shear stress is found (Perktold and Rappitsch, 1995; Rutten, 1998; Reuderink, 1991). Peripheral resistance in a CFD model can in principle be manipulated by altering the outflow boundary conditions. Recently, Augst et al. (2003) have compared three different outflow treatment schemes, showing that variation of flow patterns was strongly influenced by outflow conditions. However, wall movement was neglected in the latter study.

In the present study we systematically investigate the influence of both peripheral resistance and elasticity on CFD flow parameters. Furthermore, instead of comparing model (wall shear) stress patterns between different models (e.g. Lee et al., 2004; Marshall et al., 2004), we have compared the clinically relevant and easily obtained flow wave forms from the CFD calculations to in vivo measurements.

We have considered a human carotid bifurcation, being prone to atherosclerotic lesions. Four different carotid bifurcation models have been investigated: rigid and elastic walls, each with either traction-free outflow or positive peripheral resistance. Our hypothesis is that the best agreement in terms of flow wave forms between model and in vivo measurement will be found in the model that incorporates both elastic walls and positive peripheral resistance.

2. Methods

2.1. Ultrasound measurements

The in vivo data were obtained using an Aloka SSD-2000 ultrasound scanner, enhanced with a function to measure velocity profiles (Taniguchi et al., 1997), with a 7.5 MHz linear probe. Scanning of the right carotid artery was performed by a qualified, experienced examiner; the subject (healthy female volunteer aged 30, who gave informed consent) was lying supine with the head turned 45° from the side being scanned. The pulse repetition frequency was adapted to prevent aliasing. Per cardiac cycle, 6–18 frames were collected. Each frame was analyzed to obtain time-dependent velocity profiles. The Doppler wave form was measured at each position; all positions are named and defined in Table 1. Vessel diameters were determined from cross-sectional measurements (Table 2) assuring the oblique position of the probe by a maximum reflection from the far-wall border between lumen and intima. All measurements were repeated twice; cross-sectionally and longitudinally. The maximum and minimum diameters were determined from the frame frozen at systole and diastole, respectively.

Table 1
Ultrasound measurement positions

Name	Description	Position
DCCA	Distal common carotid artery	2 cm before bifurcation
PICA	Proximal internal carotid artery	3 cm after bulbus ('carotid sinus')
MICA	Mid-internal carotid artery	Half-way between PICA and DICA
DICA	Distal internal carotid artery	Most distal point that can be measured with angle $<60^\circ$
PECA	Proximal external carotid artery	Most proximal point without flow disturbance from bifurcation
DECA	Distal external carotid artery	Most distal point that can be measured with angle $<60^\circ$

Table 2
Measured vessel diameters (circular, except for the bifurcation, where the largest cross-sectional length was taken) and relative distensibility $(d|_{\text{systole}} - d|_{\text{diastole}})/d|_{\text{diastole}}$, where d is the diameter

Position	Distance from DCCA (cm)	Systolic diameter (cm)	Distensibility (%)
DCCA	0	0.69	16
Entrance bifurcation	2	1.21	14
ICA at apex	5	0.70	10
ECA at apex	5	0.55	10
Bulbus	7	0.80	12
PICA	10	0.63	10
DICA	14	0.50	8
PECA	7	0.42	6
DECA	11	0.35	4

2.2. Numerical model

A finite-volume cut-cell discretization of the Navier–Stokes equations on a rectilinear (Cartesian) grid was employed, thus enabling applications with arbitrary complex (3D) geometries (Dröge and Verstappen, 2005; Yokoi et al., 2005).

The fluid was considered as a homogeneous Newtonian fluid (Perktold et al., 1991) with a kinematic viscosity of $\nu = 4 \times 10^{-6}\,\mathrm{m}^2/\mathrm{s}$.

Therefore the incompressible Navier–Stokes equations were used (conservation form)

$$\int_{\partial V} \mathbf{u} \cdot \mathbf{n}\, \mathrm{d}S = 0, \tag{1}$$

$$\int_V \frac{\partial \mathbf{u}}{\partial t}\, \mathrm{d}V + \int_{\partial V} \mathbf{u}\mathbf{u}^{\mathrm{T}} \cdot \mathbf{n}\, \mathrm{d}S = -\frac{1}{\rho} \int_{\partial V} (pI_3 - \mu \nabla \mathbf{u}) \cdot \mathbf{n}\, \mathrm{d}S. \tag{2}$$

Here $\mathbf{u}$ is the velocity, ρ the pressure, μ the dynamical viscosity, ρ the density of the fluid, $\mathbf{n}$ the normal on the boundary ∂V of the control volume V and I_3 the 3×3 identity matrix.

As the boundaries will generally not coincide with grid lines, cell and edge apertures were introduced that denote the fraction of the cell that is occupied by fluid (F_b) and the fraction of a cell face that is open to flow (A_x, etc.), respectively (Figs. 1a and b); compare the 'open area ratios' of Yokoi et al. (2005). The fluid Eqs. (1) and (2) were solved following the Marker and Cell (MAC)-method (Harlow and Welch, 1965); the velocities are placed at the cell faces and the pressures at the cell centres. The finite-volume discretization of the convective and diffusive terms took account of the apertures (Appendix A). The resulting numerical method is stable (Verstappen and Veldman, 2003; Dröge and Verstappen, 2005).

2.3. Elasticity model

A relatively simple model to describe the elastic wall, assuming small longitudinal displacements, is the independent ring model (Perktold and Rappitsch, 1994; Quarteroni et al., 2000; Cebral et al., 2002):

$$\rho_{\mathrm{w}} h \frac{\partial^2 \eta}{\partial t^2} + \frac{Eh}{(1-\nu^2)R_0^2}\, \eta = p_{\mathrm{w}} - p_0, \tag{3}$$

where ρ_{w} denotes wall density, h wall thickness, η wall displacement, E Young's modulus, ν Poisson ratio, R_0 vessel radius, p_{w} fluid pressure and p_0 external pressure. This model can be extended with damping and longitudinal tension (generalized string model, Formaggia et al., 2001). The present model is chosen in the latter spirit; it is implemented here as an elastic membrane by using 3D particles connected by springs. It can be

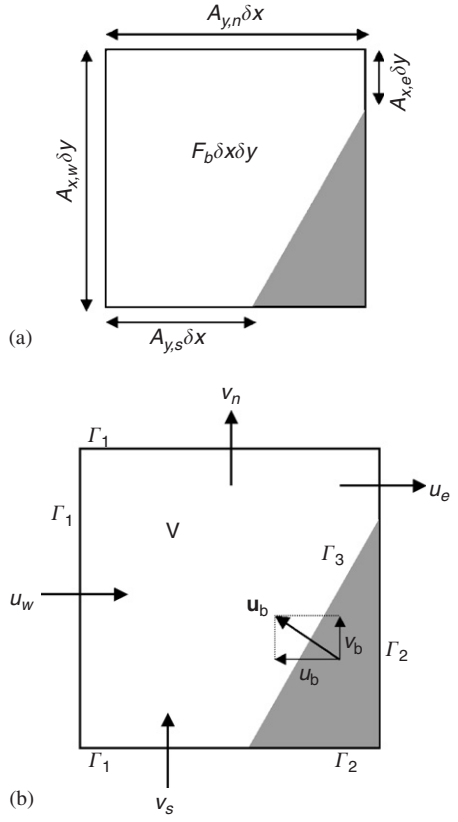

Fig. 1. Illustration of the volume and edge apertures (a) and the location of the velocities (b). The shaded area represents a solid body. Further notation used in the text is indicated in (b).

described by a momentum balance equation

$$\frac{\partial^2 \mathbf{x}}{\partial t^2} = \alpha f(\mathbf{x}) + \beta \frac{\partial \mathbf{x}}{\partial t} + F_{\mathrm{pres}}, \tag{4}$$

where $\mathbf{x}$ is the position of the particles or markers, α a spring constant, β a damping constant, and F_{pres} the force due to the transmural pressure $(p_{\mathrm{w}} - p_0)$ across the vessel wall. The first term $\alpha f(\mathbf{x})$ in (4) gives the spring force on a particle due to the presence of its neighbors. Each individual spring has its own spring constant that is tuned to match the elastic force term in the independent ring model (3) where Young's modulus is determined for each position in Table 2 from the measured diameter d at diastole and systole. The local value of α is derived as

$$\alpha = \frac{-F_{\mathrm{pres}}|_{\mathrm{systole}}}{d|_{\mathrm{systole}} - d|_{\mathrm{diastole}}}. \tag{5}$$

At intermediate positions, Young's modulus is linearly interpolated.

The parameter β is chosen as a fraction of critical damping in the one-dimensional homogeneous spring equation for each spring ($\beta_{\mathrm{crit}} = 2\sqrt{\alpha}$). The choice for β, here set at $\beta_{\mathrm{crit}}/10$, was found to be not very critical.

2.4. Fluid–structure interaction

The Navier–Stokes equations for the fluid (Eqs. (1) and (2)) and the wall equations for the structure (Eq. (3)), are solved by a weak coupling method. Each time step, first, the Navier–Stokes equations are solved in all interior fluid cells. The pressure values are then used as input for the wall equations, which then yield both the new position and the velocity of the wall. It is not obvious a priori that such an explicit coupling will be numerically stable (Loots, 2003). We verified that in our simulations the elastic wall is sufficiently stiff to ensure numerical stability of this explicit coupling. For a less stiff wall, an implicit numerical coupling per timestep would have been necessary.

2.5. Boundary conditions; treatment of peripheral resistance

The period of one cardiac cycle is chosen as 1 s, which is a good approximation to the varying cycle length during measurement. The inlet velocity is described using the ultrasound measurements at DCCA (Fig. 2).

At the outlet we prescribe $p = p_{\text{out}}$ and $\partial \mathbf{u}/\partial \mathbf{n} = 0$ (Sani and Gresho, 1994) to comply with the 'natural' traction-free boundary condition (Perktold and Rappitsch, 1995). The pressure p_{out} has to be set at three outlet boundaries: the external and internal carotid branches and the thyroid artery. Both traction-free (i.e. no additional peripheral resistance in the ECA) and positive peripheral resistance boundary conditions have been investigated.

In the traction-free outflow simulations, we set $p_{\text{out,ICA}} = p_{\text{out,ECA}} = p_0$, where p_0 equals the external pressure as in (3). If positive peripheral resistance is simulated, we set $p_{\text{out,ICA}} < p_{\text{out,ECA}}$ consistent with the experimental observation that most of the flow (ca. 65%) passes through the ICA. Because of the incompressibility of the flow, the absolute pressure level hardly influences the flow pattern. Thus varying peripheral resistance is equivalent with varying the relative outlet pressures (i.e. the pressure difference). The outflow pressure in the thyroid artery has an intermediate value, but this artery has a small impact on the overall flow pattern in the ICA due to its relatively small diameter (Zhao et al., 1999).

We have thus considered four different carotid bifurcation models: rigid walls with either traction-free outflow (model A) or positive peripheral resistance (model B), and elastic walls with either traction-free outflow (model C) or positive peripheral resistance (model D).

2.6. Computational geometry

Since flow through the superior thyroid artery (STA) was found to have a significant effect on flow patterns in the ECA (Zhao et al., 1999), and this artery originated very soon after the bifurcation in the ECA in our human volunteer, the geometry of the STA branch was also taken into account in the model.

The central axes of the carotis communis, the internal and external branch, as well as the thyroid branch were defined on the (x, y)-plane. By linear interpolation of the local radii obtained from our ultrasound measurements at the end of diastole, the radius as a function of the length of each central axis was defined. After that, the model was divided into 87 conical-shaped segments (Fig. 3).

The geometry description, consisting of the apertures, is obtained by computing for each cell and for each cell face the fraction that is inside the union of the 87 segments. Part of the 3D surface markers, including connections between segments, is shown in Fig. 4.

All methods described in this section have been validated extensively in Loots (2003).

3. Results

A complete set of measurements could be acquired at PECA and DECA. Although velocity profiles from both PICA and DICA were obtained, in the ICA, a complete

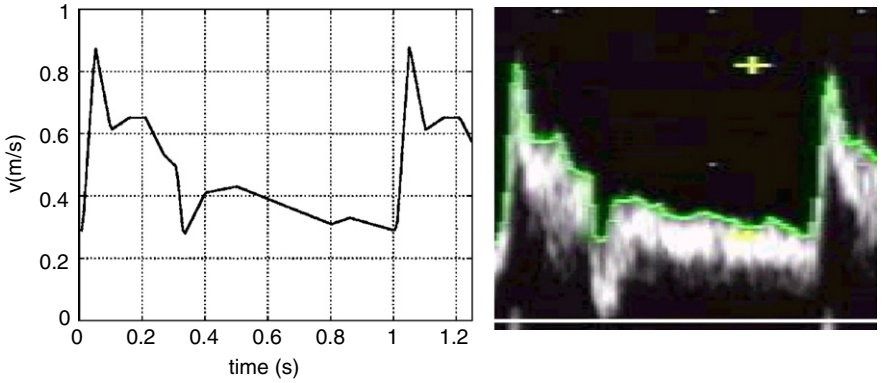

Fig. 2. Left: the input signal v_{in} at DCCA. Right: measured flow wave form at DCCA at the same vertical and horizontal scale as on the left.

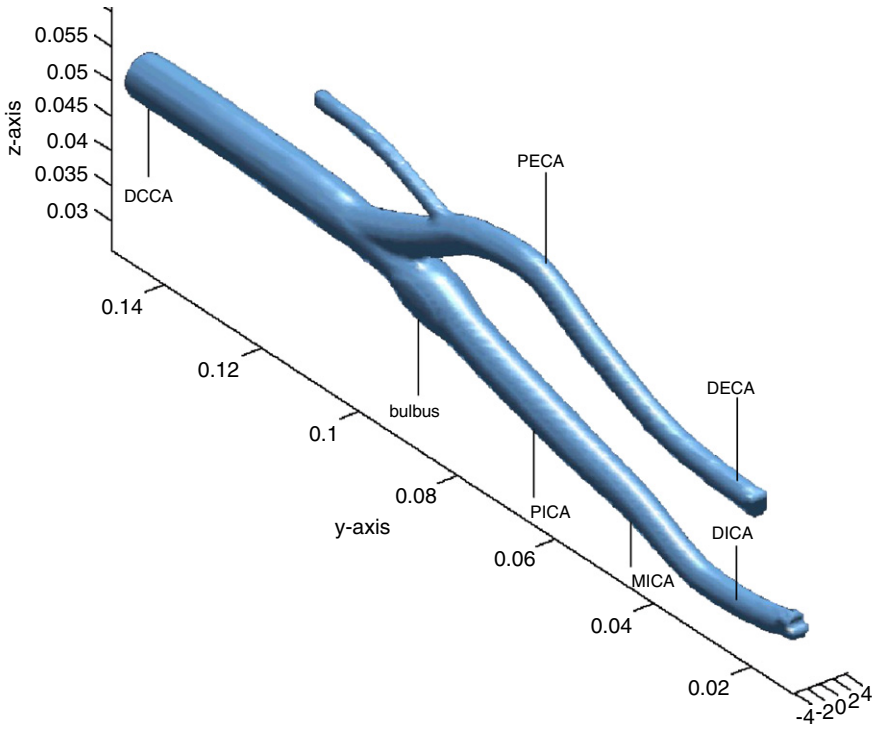

Fig. 3. A 3D view of the model for the carotid bifurcation.

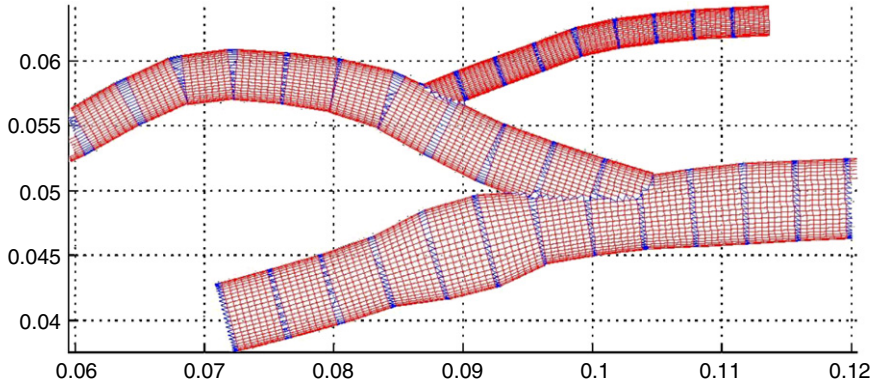

Fig. 4. Partial geometry covered with markers and elastic springs at diastole. Units are meters.

data set could only be collected from MICA (between PICA and DICA, see Fig. 3). In Table 3, the measured and calculated systolic, diastolic and mean velocities are given.

3.1. Flow wave forms

In general, the velocities increase between PECA and DECA in all four models, as a direct consequence of the decrease in diameter (and area) in downstream direction. The radius decreases from 2.1 mm at PECA to 1.75 mm at DECA, leading to a 50–60% increase of the velocity (Table 3).

The systolic velocities are overestimated in the rigid models A and B. This effect is strongest in model A, at DECA. Adding peripheral resistance (model B) leads to similar velocities in the ICA, but has a profoundly decreasing effect on velocities in the ECA; yet, the latter velocities are still higher than measured. Diastolic ECA velocities are similar to measured velocities in model B.

Models C and D provide elastic geometries. The elasticity decreases in downstream direction, mostly in the external branch. This is well-known from in vivo measurements (Reneman et al., 1996) and was also found in our measurements of the distensibility (Table 2). In both models C and D, the systolic velocities are much more comparable to measured velocities than in the rigid models. However, the systolic velocity is still slightly overestimated at DECA, even in the model with

Table 3
Systolic (max.), diastolic (min.) and time-averaged mean (mean) velocities and pulsatility index (PI = max–min/mean) resulting from the in vivo measurement (top) and the four numerical experiments (bottom)

Measurement			Position							
			MICA			PECA			DECA	
Max			0.85			0.62			0.71	
Min			0.37			0.08			0.11	
Mean			0.52			0.14			0.23	
PI			0.92			3.86			2.61	
Model calculations		Rigid				Elastic				
		Position								
			MICA	PECA	DECA			MICA	PECA	DECA
Traction free	Model A	Max	0.91	0.84	1.33	Model C	Max	0.73	0.65	0.97
		Min	0.31	0.30	0.45		Min	0.35	0.31	0.50
		Mean	0.47	0.45	0.69		Mean	0.45	0.41	0.66
		PI	1.28	1.20	1.28		PI	0.84	0.83	0.71
Peripheral Resistance	Model B	Max	0.96	0.76	1.22	Model D	Max	0.93	0.54	0.87
		Min	0.41	0.09	0.13		Min	0.43	0.09	0.14
		Mean	0.55	0.30	0.45		Mean	0.62	0.20	0.33
		PI	1.00	2.23	2.42		PI	0.81	2.25	2.21

A: rigid walls, traction-free outflow, B: rigid walls, positive peripheral resistance, C: elastic walls, traction-free outflow, D: elastic walls, positive peripheral resistance. Velocities are given in m/s.
Definitions of measurement positions are given in Table 1.

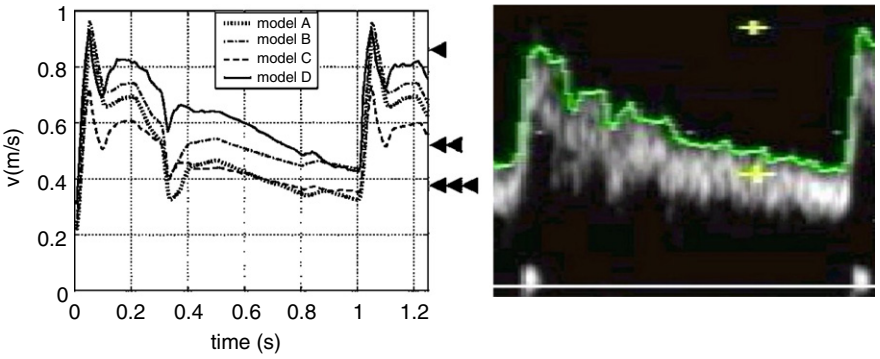

Fig. 5. Left: flow wave forms for the four models at MICA. Right: measured flow wave form at the same vertical scale as on the left. (◀) Measured systolic velocity, (◀◀) measured mean velocity, and (◀◀◀) measured diastolic velocity.

positive peripheral resistance (model D). The effect of positive peripheral resistance can be clearly seen; ICA velocities increase whereas ECA velocities decrease, most strongly for diastolic and mean velocities. This effect is visible both in the rigid and elastic models. As an effect of peripheral resistance the flow through the externa is reduced by a third.

In Figs. 5–7, the measured and calculated flow wave forms, during 1.25 cardiac cycles are shown at MICA, PECA and DECA. For all models, the shape of the flow wave forms is very similar to that of the inflow pulse (Fig. 2). At MICA the direct influence of the inflow pulse, which reflects the mechanical heart action, is largely preserved, independent of the model. At DECA and PECA the combination of elastic vessel walls and peripheral resistance (model D) lowers the velocity outside the systolic phase considerably. Elasticity alone (model C) does not sufficiently dampen the velocities in the diastolic phase, but does lead to more realistic systolic velocities. The damping of the velocities due to elasticity is reflected in the flow wave form shape during the entire pulse: peaks and valleys are less sharp (models C and D). At all three positions in the carotid bifurcation the best similarity in shape between the measured flow wave forms and the model flow wave forms is obtained for model D.

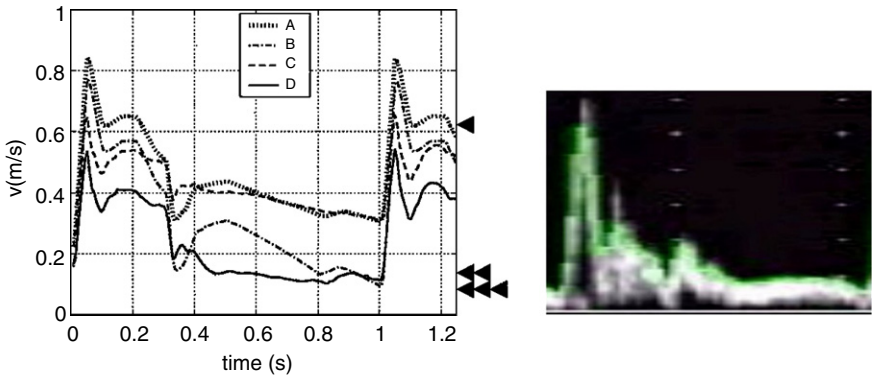

Fig. 6. Left: flow wave forms for the four models at PECA. Right: measured flow wave form at the same vertical scale as on the left. (◀) Measured systolic velocity, (◀◀) measured mean velocity, and (◀◀◀) measured diastolic velocity.

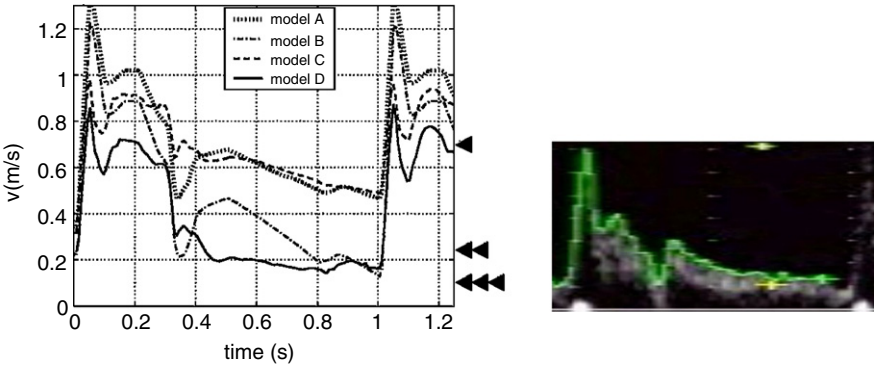

Fig. 7. Left: flow wave forms for the four models at DECA. Right: measured flow wave form at the same vertical scale as on the left. (◀) Measured systolic velocity, (◀◀) measured mean velocity, and (◀◀◀) measured diastolic velocity.

3.2. Velocity profiles

Measured and computed (model D) velocity profiles are shown in Figs. 8 and 9. All profiles are strongly skewed. For PICA and DICA, the maximum is located on the right, near the flow-divider wall. The profile at PECA is also maximal near the flow-divider wall, while at DECA the large velocities have shifted side. This can all be explained by the carotid branch curvatures. Measured and model velocity profiles are qualitatively similar. They are block-shaped due to the non-stationarity of the flow which can be expressed in the Womersley number $\alpha_W = R\sqrt{\omega/\nu}$. Here, the radius $R = 3\,\text{mm}$ and angular frequency $\omega = 2\pi f = 2\pi$, yielding $\alpha_W = 4.3$. This value for α_W is clearly outside the quasi-stationary range $\alpha_W < 1$, explaining the non-parabolical appearance of the measured velocity profiles.

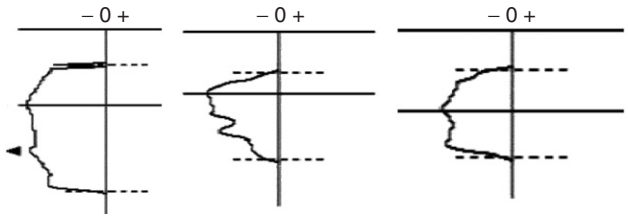

Fig. 8. Measured velocity profiles at systole, left: DCCA, middle: DICA and right: PECA.

4. Discussion

In this paper, we have systematically investigated the influence of peripheral resistance and elasticity on the Doppler flow wave forms obtained from a CFD-model of the carotid bifurcation, by comparing the results to in vivo ultrasound measurements.

Ultrasound was used to obtain the geometry and elasticities, the Doppler flow wave forms and velocity profiles, because it is a fast and non-invasive method. Our observed diameters and distensibilities are similar to values found in literature for the same sex and age group (Müller et al., 1987; Schöning et al., 1994; Hansen et al., 1995; Meyer et al., 1997).

Peripheral resistance—being the ratio between perfusion pressure and flow—can be measured non-invasively in the carotid arteries using applanation tonometry, but it is difficult to obtain a reliable value for the local

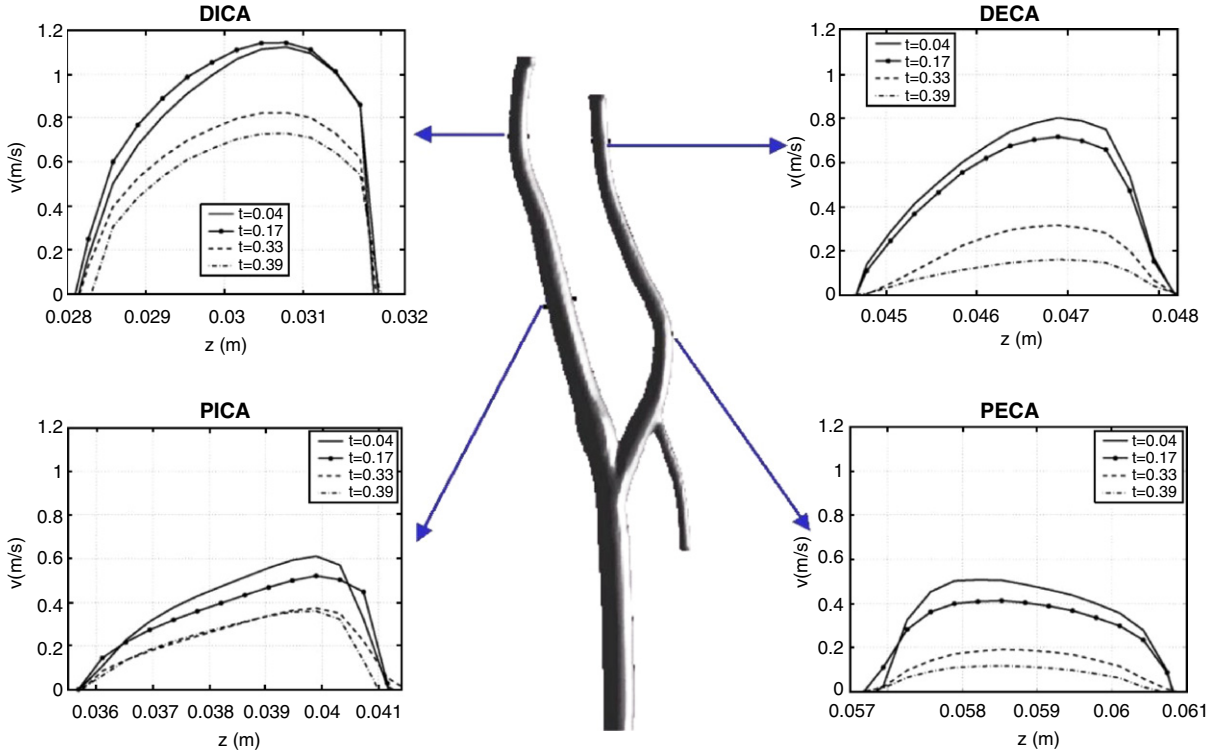

Fig. 9. Calculated velocity profiles for model D and their positions in the geometry.

perfusion pressure (Bella et al., 1999; van Bortel et al., 2001). Peripheral resistance has succesfully been determined in vivo in the brachial artery however (Legarth and Nolsoe, 1990). These in vivo measurements, and model calculations (Legarth and Thorup, 1989), have shown that peripheral resistance is linearly related to the PI, which can be directly derived from the Doppler wave form. The clinical importance of the PI is a reflection of the fact that downstream arterial structures largely determine the upstream flow phenomena. We have therefore represented peripheral resistance by prescribing different, constant pressure levels at the ICA and ECA outflow boundaries.

Most recent CFD simulations of carotid bifurcations also employ boundary conditions in which higher peripheral resistance in the ECA is taken into account by imposing the observed (variable) flow division ratio in the two branches (Marshall et al., 2004; Lee et al., 2004). This type of boundary condition—but only when elasticity is taken into account as well—can now be concluded to be essential for a good correspondence between CFD results and in vivo measurements. As pointed out by Augst et al. (2003), it is not sufficient to only take the flow division ratio into account according to the cross-sectional areas of both branches. From our study it can now be understood, that this would effectively be a completely traction-free simulation.

In the simulations presented, the peripheral pressure values are taken constant in time. In the absence of elasticity, time-dependent peripheral pressure boundary conditions will only change the pressure level and leave the flow pattern unaffected (because of the incompressibility of the flow). We therefore expect that in the presence of elasticity, effects of time-dependent peripheral pressure boundary conditions on the flow pattern will be small. This is currently under investigation by coupling our Navier–Stokes model to a lumped parameter model for the circulation.

The computed peak systolic velocities are considerably lower and a more realistic smoothing of the flow wave form is found, if elasticity is taken into account. This was also found by others (Perktold and Rappitsch, 1995; Hofer et al., 1996; Zhao et al., 2000) and is corroborated by the fact that peak systolic velocities generally increase in older people, mainly due to degenerative elasticity loss (von Reutern and von Büdingen, 1993). Our results show that the flow velocities outside systole are hardly influenced by elasticity. The incorporation of peripheral resistance mainly influences the diastolic and mean flow velocities; both are increased in the ICA and decreased in the ECA if peripheral resistance is taken into account. This phenomenon is also found in pathology. In case of increased downstream pressure, especially the diastolic and mean velocities are known to decrease, whereas the systolic peak velocity can be preserved for a long time.

In order to obtain an even better agreement between experiment and simulation, it may be important to

improve upon the accuracy of the measurements. The strong downstream decrease in the ICA and ECA diameters that we found, may be overestimated. The diameters of the distal positions may not be measured with maximum accuracy, mainly because the curvature of the vessels was such that an insonation angle between 30° and 60° was hard to obtain. Errors in the model elasticity parameters α and β can cause changes in the delay between maximum pressure and maximum wall extension. We intend to study other normal controls, of different ages, to evaluate the influence of these experimental measurement errors.

In conclusion, we have shown that only if both physical elasticity and peripheral resistance are taken into account, a close resemblance between the Doppler flow wave forms obtained from ultrasound experiments and the flow wave forms from numerical calculations can be obtained.

Acknowledgement

We thank Dr. J.H. van der Hoeven for valuable comments and E.B. Muskens and A.T.B. van Loon for their technical assistance.

Appendix A

The discretization in case of moving walls can be explained with Fig. 1, where the open part of the computational cell serves as a control volume (for clarity of presentation it is taken 2D).

Applying mass conservation and using terminology defined in Fig. 1b Eq. (1) gives

$$\int_{\Gamma_1} \mathbf{u}\cdot\mathbf{n}\,\mathrm{d}S + \int_{\Gamma_3} \mathbf{u}_\mathrm{b}\cdot\mathbf{n}\,\mathrm{d}S = 0. \tag{A.1}$$

Since $\mathbf{u}_\mathrm{b}$ corresponds with solid-body motion of the cut-off part of the cell, the boundary integral along Γ_3 can be rewritten along Γ_2, yielding

$$\int_{\Gamma_1} \mathbf{u}\cdot\mathbf{n}\,\mathrm{d}S + \int_{\Gamma_2} \mathbf{u}_\mathrm{b}\cdot\mathbf{n}\,\mathrm{d}S = 0. \tag{A.2}$$

Expressed in cell apertures (Fig. 1a) and numerical velocities $\mathbf{u}=(u,v)$ and $\mathbf{u}_\mathrm{b}=(u_\mathrm{b},\ v_\mathrm{b})$ (Fig. 1b) this results in

$$\begin{aligned} &-A_{x,\mathrm{w}}\,\delta y\,u_\mathrm{w} + A_{y,\mathrm{n}}\,\delta x\,v_\mathrm{n} - A_{y,\mathrm{s}}\,\delta x\,v_\mathrm{s} + A_{x,\mathrm{e}}\,\delta y\,u_\mathrm{e} \\ &\quad -(1-A_{y,\mathrm{s}})\delta x\,v_\mathrm{b} + (1-A_{x,\mathrm{e}})\delta y\,u_\mathrm{b} = 0. \end{aligned} \tag{A.3}$$

For the momentum equations, similar alterations concerning the moving wall have to be taken into account. For details see Loots et al. (2003) and Loots (2003).

References

Augst, A.D., Barratt, D.C., Hughes, A.D., Thom, S.A.M., Xu, X.Y., 2003. Various issues relating to computational fluid dynamics simulations of carotid bifurcation flow based on models reconstructed from three-dimensional ultrasound images. Proceedings of the Institution of Mechanical Engineers Part H-Journal of Engineering in Medicine 217, 393–403.

Bella, J.N., Roman, M.J., Pini, R., Schwartz, J.E., Pickering, T.G., Devereux, R.B., 1999. Assessment of arterial compliance by carotid midwall strain–stress relation in hypertension. Hypertension 33, 793–799.

Cebral, J.R., Yim, P.J., Lohner, R., Soto, O., Choyke, P.L., 2002. Blood flow modeling in carotid arteries with computational fluid dynamics and MR imaging. Academic Radiology 9, 1286–1299.

Dröge, M.T., Verstappen, R.W.C.P., 2005. A new symmetry-preserving Cartesian-grid method for computing flow past arbitrarily shaped objects. International Journal for Numerical Methods in Fluids 47, 979–985.

Formaggia, L., Gerbeau, J.F., Nobile, F., Quarteroni, A., 2001. On the coupling of 3D and 1D Navier–Stokes equations for flow problems in compliant vessels. Computer Methods in Applied Mechanics and Engineering 191, 561–582.

Hansen, F., Mangell, P., Sonesson, B., Lanne, T., 1995. Diameter and compliance in the human common carotid-artery—variations with age and sex. Ultrasound in Medicine and Biology 21, 1–9.

Harlow, F.H., Welch, J.E., 1965. Numerical calculation of time-dependent viscous incompressible flow of fluid with free surface. Physics of Fluids 8, 2182–2189.

Hofer, M., Rappitsch, G., Perktold, K., Trubel, W., Schima, H., 1996. Numerical study of wall mechanics and fluid dynamics in end-to-side anastomoses and correlation to intimal hyperplasia. Journal of Biomechanics 29, 1297–1308.

Kleinstreuer, C., Buchanan, J.R., Lei, M., Truskey, G.A., 2001. Computational analysis of particle-hemodynamics and prediction of the onset of arterial diseases. In: Leondes, C. (Ed.), Cardiovascular Techniques. Biomechanical Systems, Techniques and Applications. CRC Press, London, pp. 1–69.

Ku, D.N., 1997. Blood flow in arteries. Annual Review of Fluid Mechanics 29, 399–434.

Lee, K.W., Wood, N.B., Xu, X.Y., 2004. Ultrasound image-based computer model of a common carotid artery with a plaque. Medical Engineering and Physics 26, 823–840.

Legarth, J., Nolsoe, C., 1990. Doppler blood velocity wave-forms and the relation to peripheral resistance in the brachial-artery. Journal of Ultrasound in Medicine 9, 449–453.

Legarth, J., Thorup, E., 1989. Characteristics of Doppler blood-velocity waveforms in a cardiovascular invitro model. 2. The influence of peripheral resistance, perfusion-pressure and blood-flow. Scandinavian Journal of Clinical and Laboratory Investigation 49, 459–464.

Long, Q., Xu, X.Y., Ariff, B., Thom, S.A., Hughes, A.D., Stanton, A.V., 2000. Reconstruction of blood flow patterns in a human carotid bifurcation: a combined CFD and MRI study. Journal of Magnetic Resonance Imaging 11, 299–311.

Loots, G.E., 2003. Fluid–structure interaction in hemodynamics. Ph.D. Thesis, Groningen University, The Netherlands.

Loots, E., Hillen, B., Veldman, A.E.P., 2003. The role of hemodynamics in the development of the outflow tract of the heart. Journal of Engineering Mathematics 45, 91–104.

Marshall, I., Zhao, S.Z., Papathanasopoulou, P., Hoskins, P., Xu, X.Y., 2004. MRI and CFD studies of pulsatile flow in healthy and stenosed carotid bifurcation models. Journal of Biomechanics 37, 679–687.

Meyer, J.I., Khalil, R.M., Obuchowski, N.A., Baus, L.K., 1997. Common carotid artery: variability of Doppler US velocity measurements. Radiology 204, 339–341.

Milner, J.S., Moore, J.A., Rutt, B.K., Steinman, D.A., 1998. Hemodynamics of human carotid artery bifurcations: computational studies with models reconstructed from magnetic resonance imaging of normal subjects. Journal of Vascular Surgery 28, 143–156.

Moore, J.A., Steinman, D.A., Holdsworth, D.W., Ethier, C.R., 1999. Accuracy of computational hemodynamics in complex arterial geometries reconstructed from magnetic resonance imaging. Annals of Biomedical Engineering 27, 32–41.

Müller, H.R., Radue, E.W., Buser, M., 1987. Cranial blood flow measurement by means of Doppler ultrasound. In: Spencer, M.P. (Ed.), Ultrasonic Diagnosis of Cerebrovascular Disease. Nijhoff, Dordrecht, pp. 87–102.

Perktold, K., Rappitsch, G., 1994. Mathematical modeling of local arterial flow and vessel mechanics. In: Crolet, J.-M., Ohayon, R. (Eds.), Computational Methods for Fluid–structure Interaction. Wiley, New York, pp. 230–245.

Perktold, K., Rappitsch, G., 1995. Computer-simulation of local blood-flow and vessel mechanics in a compliant carotid-artery bifurcation model. Journal of Biomechanics 28, 845–856.

Perktold, K., Resch, M., Florian, H., 1991. Pulsatile non-Newtonian flow characteristics in a 3-dimensional human carotid bifurcation model. Journal of Biomechanical Engineering-Transactions of the ASME 113, 464–475.

Quarteroni, A., Tuveri, M., Veneziani, A., 2000. Computational vascular fluid dynamics: problems, models and methods. Computing and Visualization in Science 2, 163–197.

Reneman, R.S., Hoeks, A.P.G., Westerhof, N., 1996. Non-invasive assessment of artery wall properties in humans—methods and interpretation. Journal of Vascular Investigation 2, 53–64.

Reuderink, P., 1991. Analysis of the flow in a 3D distensible model of the carotid artery bifurcation. Ph.D. Thesis, Eindhoven University of Technology, The Netherlands.

Ross, R., 1993. The pathogenesis of atherosclerosis—a perspective for the 1990s. Nature 362, 801–809.

Rutten, M., 1998. Fluid–solid interaction in large arteries. Ph.D. Thesis, Eindhoven University of Technology, The Netherlands.

Sani, R.L., Gresho, P.M., 1994. Resume and remarks on the open boundary condition minisymposium. International Journal for Numerical Methods in Fluids 18, 983–1008.

Schöning, M., Walter, J., Scheel, P., 1994. Estimation of cerebral blood-flow through color duplex sonography of the carotid and vertebral arteries in healthy-adults. Stroke 25, 17–22.

Taniguchi, N., Itoh, K., Takano, R., Yasuda, Y., Asano, Y., 1997. Measurement of blood flow via velocity profiles using color Doppler signals. Ultrasound International 3, 127–133.

van Bortel, L.M., Balkestein, E.J., van der Heijden-Spek, J.J., Vanmolkot, F.H., Staessen, J.A., Kragten, J.A., Vredeveld, J.W., Safar, M.E., Struijker Boudier, H.A., Hoeks, A.P., 2001. Non-invasive assessment of local arterial pulse pressure: comparison of applanation tonometry and echo-tracking. Journal of Hypertension 19, 1037–1044.

Verstappen, R.W.C.P., Veldman, A.E.P., 2003. Symmetry-preserving discretisation of turbulent flow. Journal of Computational Physics 187, 343–368.

von Reutern, G.M., von Büdingen, H.J., 1993. Ultrasound Diagnosis of Cerebrovascular Disease. Georg Thieme Verlag, Stuttgart.

Yokoi, K., Xiao, F., Liu, H., Fukasaku, K., 2005. Three-dimensional numerical simulation of flows with complex geometries in a regular Cartesian grid and its application to blood flow in cerebral artery with multiple aneurysms. Journal of Computational Physics 202, 1–19.

Zhao, S.Z., Xu, X.Y., Collins, M.W., Stanton, A.V., Hughes, A.D., Thom, S.A., 1999. Flow in carotid bifurcations: effect of the superior thyroid artery. Medical Engineering and Physics 21, 207–214.

Zhao, S.Z., Xu, X.Y., Hughes, A.D., Thom, S.A., Stanton, A.V., Ariff, B., Long, Q., 2000. Blood flow and vessel mechanics in a physiologically realistic model of a human carotid arterial bifurcation. Journal of Biomechanics 33, 975–984.